NMR Line Shape of Rotating ^{3}He-B at Large Counterflow Velocity

J. Kopu*, R. Schanen†, R. Blaauwgeers‡, V. B. Eltsov§,
M. Krusius, J. J. Ruohio, and E. V. Thuneberg
Low Temperature Laboratory, Helsinki University of Technology, Finland

27 April 2000

Abstract

We have investigated the NMR line shapes of superfluid ^{3}He-B in a rotating cylinder. In the vortex-free state at sufficiently large angular velocity of rotation, $\Omega \gtrsim 1$ rad/s, the main feature of the absorption spectrum is a large frequency-shifted peak above the Larmor frequency. The shape of this counterflow peak is both measured and calculated as a function of external magnetic field strength, angular velocity, temperature, and number of vortex lines. The NMR spectrum is derived from the calculated order-parameter texture. Reasonable agreement with the measured line shape is obtained by including line-broadening effects due to the external field inhomogeneity and Leggett-Takagi relaxation.

1 Introduction

Superfluids attempt to respond to rotation by forming quantized vortex lines. However, because of the high critical velocity, superfluid ^{3}He-B can form a vortex-free state in rotation (the equivalent of the Meissner state in superconductors) or other metastable states with less vortices than the equilibrium number [1]. In a cylindrical container, the existing vortex lines are accumulated in a central bundle and are surrounded by a region of nonzero

*e-mail: juha.kopu@hut.fi
†Also at CRTBT-CNRS, Grenoble, France.
‡Also at Kamerlingh Onnes Laboratory, Leiden University, The Netherlands.
§Also at Kapitza Institute for Physical Problems, Moscow, Russia.

counterflow. The presence of the vortex lines can be detected because of a specific signature in the NMR absorption signal. It has been a longstanding goal for experimentalists to observe the formation and annihilation of single vortex lines in superfluid ^{3}He [2]. This objective requires a thorough understanding of NMR line shapes and signal optimization, and provides the main motivation for this paper.

A second motivation has been to test how well the experimental properties of ^{3}He-B can be understood using the weak-coupling quasiclassical theory [3]. The theoretical determination of the NMR response of ^{3}He-B is done in three steps. The first step is to calculate the hydrostatic coefficients of ^{3}He-B. These coefficients have been worked out in Ref. [4] using the weak-coupling quasiclassical theory. The second step is to determine the texture of the order parameter using the hydrostatic theory. In this paper we have calculated the texture in a cylindrical container using both 1D and 2D models. These two steps give a definite prediction how the texture depends on external parameters such as the temperature, pressure, magnetic field, and rotation, and also on the number of vortices in the container. The texture immediately gives the ideal NMR spectrum. The final third step is to add additional line broadening to the ideal spectrum. We concentrate on the case of high counterflow velocities. In this case, as will be shown in the paper, the inhomogeneity of the magnetic field and the intrinsic Leggett-Takagi relaxation have to be taken into account.

At high rotation velocities in the vortex-free state the NMR response consists of one large peak at a frequency slightly above the Larmor value. This report contains a study of how the height of this counterflow peak depends on different external parameters and on the number of vortices in the container. The counterflow peak heights have been determined both experimentally and theoretically. Comparison of the two gives good agreement and allows us to extract an estimate for the Leggett-Takagi relaxation time $\tau_{\rm LT}$. The optimal conditions for measuring single-vortex events are analyzed.

A thorough introduction to textures in a rotating container has been previously given in Refs. [5] and [6]. Part of the introduction is repeated here because our approach differs in several details.

2 Hydrostatic theory

The order parameter in unperturbed bulk B phase has the form of a rotation matrix $\overleftrightarrow{\rm R}(\hat{\mathbf{n}}, \theta)$. The interaction between the nuclear dipole mo-

ments of the helium atoms fixes the rotation angle θ to $\arccos(-1/4)$ [7]. Therefore the order parameter texture is given by the spatial distribution of a unit vector $\hat{\mathbf{n}}(\mathbf{r})$. Because our experimental container is a cylinder, we choose to write the vector in cylindrical coordinates using two angles, $\hat{\mathbf{n}} = (-\hat{\mathbf{r}}\cos\alpha + \hat{\boldsymbol{\phi}}\sin\alpha)\sin\beta + \hat{\mathbf{z}}\cos\beta$, with $\hat{\mathbf{z}}$ parallel to the cylinder axis. The equilibrium texture can be determined by minimizing the hydrostatic free-energy functional, which in the vortex-free case consists of the following main contributions [8, 9, 10, 11]: the interaction with the external magnetic field $\mathbf{H}$

$$F_{\rm DH} = -a \int d^3\mathbf{r}\ (\hat{\mathbf{n}}\cdot\mathbf{H})^2, \tag{1}$$

the orienting energy of counterflow ($\mathbf{v} \equiv \mathbf{v}_{\rm n} - \mathbf{v}_{\rm s}$ is the velocity of counterflow, where the velocity of the normal component $\mathbf{v}_{\rm n} = \boldsymbol{\Omega}\times\mathbf{r}$ and that of the superfluid component $\mathbf{v}_{\rm s} = 0$ in the vortex-free state)

$$F_{\rm HV} = -\lambda_{\rm HV} \int d^3\mathbf{r}\ (\mathbf{H}\cdot\overleftrightarrow{\rm R}\cdot\mathbf{v})^2, \tag{2}$$

and the surface energy ($\hat{\mathbf{s}}$ is the surface normal)

$$F_{\rm SH} = -d \int d^2\mathbf{r}\ (\mathbf{H}\cdot\overleftrightarrow{\rm R}\cdot\hat{\mathbf{s}})^2. \tag{3}$$

It is conventional to define the dipolar velocity $v_{\rm D} \equiv \sqrt{2a/(5\lambda_{\rm HV})}$. All the experiments described in this paper were performed in axial field $\mathbf{H} \parallel \hat{\mathbf{z}}$. The conflicting orienting effects (e.g. F_H prefers $\hat{\mathbf{n}} \parallel \mathbf{H}$, i.e. $\beta = 0$, whereas $F_{\rm HV}$ favors an orientation corresponding to $\sin^2\beta = 0.8$) result in an inhomogeneous order-parameter texture. The gradient energy

$$F_{\rm G} = \int d^3\mathbf{r} \left[\lambda_{\rm G1}\partial_i \overleftrightarrow{\rm R}_{\alpha j}\ \partial_i \overleftrightarrow{\rm R}_{\alpha j} + \lambda_{\rm G2}\partial_i \overleftrightarrow{\rm R}_{\alpha i}\ \partial_j \overleftrightarrow{\rm R}_{\alpha j}\right] \tag{4}$$

describes the rigidity of the order parameter and opposes any bending of $\hat{\mathbf{n}}$. The length scale of the spatial variations is set by the magnetic coherence length $\xi_{\rm H} \equiv \sqrt{65\lambda_{\rm G2}/(8aH^2)}$, which is inversely proportional to the external field strength. In our experiments $\xi_{\rm H} \sim 1$ mm. In Eq. (4) we have neglected the pure divergence contribution to the gradient energy. However, for all the calculated results reported in this article, the error in the NMR peak height due to this simplification was found to be less than 3 percent.

The equilibrium textures relevant to our experimental conditions are axisymmetric, of the so-called "flare-out" form [9]. On increasing the angular

velocity of rotation Ω in the vortex-free case [1, 12] (thus increasing $v_{\rm n} = \Omega r$ and the counterflow), a succession of transitions between different types of textures occurs [13]. At the cylinder axis the magnetic field orients $\hat{\mathbf{n}}$ parallel to $\hat{\mathbf{z}}$, i.e. $\beta = 0$. When moving away from the axis β tends towards the wall- and flow-dominated value $\beta = 63.4°$ (even though the preferred α angle is different for $F_{\rm HV}$ and $F_{\rm SH}$). At sufficiently high rotation velocities, $\Omega \gtrsim 0.8$ rad/s, most of the texture (excluding regions in the vicinity of the axis and the top and the bottom of the cylinder) is oriented at this value. This is known as the crowned flare-out texture [13], and is presented in Fig. 1. It is also the preferred state for single-vortex measurements.

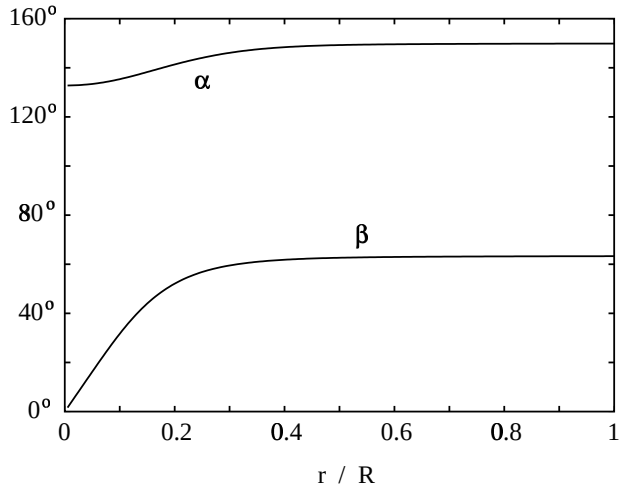

Figure 1: Numerically calculated high velocity $\hat{\mathbf{n}}$ texture in an infinitely long cylinder as a function of the distance from the axis. The radius of the sample cylinder is $R = 2.5$ mm, pressure $P = 2$ bar, $\Omega = 1.5$ rad/s, temperature $T = 0.81\ T_{\rm c}$, $H = 30$ mT, giving $\xi_{\rm H} = 0.25\ R$, $v_{\rm D} = 0.18$ mm/s, $d/a = 5.9$ mm, and $\lambda_{\rm G1}/\lambda_{\rm G2} = 1.9$.

The presence of a vortex bundle in the cylinder causes some modifications to the texture. The orbital anisotropy effect associated with the singular vortex cores can be taken into account by adding another free-energy term of the form [14, 6]

$$F_{\rm LH} = \lambda_{\rm LH} \int_{\rm B} d^3\mathbf{r}\, (\mathbf{H}\cdot \overleftrightarrow{\rm R} \cdot \hat{\mathbf{z}})^2, \tag{5}$$

where the integration is over the bundle volume. Furthermore, there is a nonvanishing superfluid velocity field around the bundle which is caused by the vortices. Inside the bundle, the average superfluid velocity $\langle \mathbf{v}_{\rm s} \rangle \approx \mathbf{v}_{\rm n}$ and the average counterflow velocity is zero, whereas in the vortex-free counterflow annulus $v(r) = \Omega r - \Omega_{\rm v} R^2/r$, where $\Omega_{\rm v} = \Omega N/N_0$, R is the radius of the sample cylinder, N is the number of vortices in the bundle, and N_0 is the vortex number for the completely filled container (vortices distributed with equilibrium density).

The phenomenological coefficients a, $\lambda_{\rm HV}$, d, $\lambda_{\rm G1}$, $\lambda_{\rm G2}$ and $\lambda_{\rm LH}$ in Eqs. (1)-(5) can be determined from the quasiclassical theory of ^{3}He [3]. We use expressions calculated with weak-coupling quasiclassical theory, which are presented in Ref. [4]. We take into account so-called "trivial" strong-coupling corrections, i.e. the energy gap used in evaluating all coefficients is enhanced from the weak coupling value as prescribed in Ref. [3]. The surface energy coefficient d is evaluated in the Ginzburg-Landau temperature regime for a diffusively scattering surface and extrapolated to lower temperatures. The vortex-core contribution has been neglected in calculating $\lambda_{\rm LH}$. It should be emphasized that the calculations in the present report contain no adjustable parameters. We use here values which are obtained directly from the formulas in Ref. [4]. The texture parameters depend only on relatively well-known quantities like the density of the liquid, the superfluid transition temperature $T_{\rm c}$, the Fermi-liquid parameters, the dipole-dipole interaction coefficient $g_{\rm D}$, and the jump of the specific heat at $T_{\rm c}$. There is some uncertainty about $g_{\rm D}$ at low pressures [4]. For consistency, we have used a value based on transverse NMR since also the temperature is measured according to that (Sect. 6).

3 Nuclear magnetic resonance

The NMR response of ^{3}He-B, in the absence of relaxation, is given by the Leggett equations [15] for small rotations $\boldsymbol{\theta}$ of the spin part of the order parameter and the spin density $\mathbf{S}$

$$\frac{\partial \boldsymbol{\theta}}{\partial t} = -\gamma \mathbf{H}_{\rm tot} + \frac{\gamma^2}{\chi_{\rm B}} \mathbf{S}, \tag{6a}$$

$$\frac{\partial \mathbf{S}}{\partial t} = \gamma \mathbf{S} \times \mathbf{H}_{\rm tot} - \frac{\chi_{\rm B}}{\gamma^2} \Omega_{\rm B}^2 \hat{\mathbf{n}} (\hat{\mathbf{n}} \cdot \boldsymbol{\theta}), \tag{6b}$$

where γ is the gyromagnetic ratio of the ^{3}He nucleus, $\chi_{\rm B}$ is the B-phase susceptibility, and $\Omega_{\rm B}$ is the B-phase longitudinal resonance frequency. $\mathbf{H}_{\rm tot}$ is the total external magnetic field consisting of the static field $\mathbf{H}$ and the small rf field $\mathbf{H'} \propto e^{i\omega t}$. The linear NMR state of transverse resonance at low excitation level H' consists of small variations about the equilibrium state, and can be written in the high-field limit in the approximate form

$$\omega \approx \sqrt{\omega_0^2 + \Omega_{\rm B}^2 \sin^2 \beta} \approx \omega_0 + \frac{\Omega_{\rm B}^2}{2\omega_0} \sin^2 \beta, \tag{7}$$

where $\omega_0 = \gamma H$ is the Larmor frequency. That is, the resonance frequency is shifted from the Larmor value only when $\hat{\mathbf{n}}$ is not parallel to $\hat{\mathbf{z}}$, and the shift is always positive. The overall spectrum is obtained by considering the fluid as an assembly of uncoupled oscillators with frequencies determined by the local value of $\beta(\mathbf{r})$ according to (7). We then obtain the NMR line shape as a distribution of the individual contributions, i.e.

$$f(\omega) = \frac{1}{V} \int d^3\mathbf{r}\ \delta[\omega - \omega(\mathbf{r})], \tag{8}$$

where V is the volume of the sample. From this so-called local oscillator model it follows that whenever $\omega(\mathbf{r})$, or equivalently, $\beta(\mathbf{r})$, has a constant value over a larger region, the absorption spectrum has a peak at this frequency. At low rotation velocities, most of the absorption occurs at frequencies close to the value $\beta = 0$. In this case the spectrum has a peak bordering to the Larmor frequency, with a tail caused by the bending of $\hat{\mathbf{n}}$ towards the boundary value $\beta = \arcsin(\sqrt{4/5}) \approx 63.4^\circ$ close to the cylinder wall. As the rotation velocity is increased in the vortex-free state, the absorption begins to accumulate towards the flow-dominated value $\beta \approx 63.4^\circ$, giving rise to a new peak in the spectrum. Finally, at high rotation velocities Ω, essentially all absorption has been shifted in the counterflow peak. Fig. 2 shows examples of typical line shapes for low ($\Omega R \ll v_{\rm D}$), intermediate ($\Omega R \sim v_{\rm D}$), and high values of Ω ($\Omega R \gg v_{\rm D}$).

In using the local oscillator model we neglect the possibility of having coherent spin motion. A more detailed study of the NMR behaviour of ^{3}He-B in a cylindrical container would require solving a Schrödinger-like equation with a space-dependent potential $\sin^2 \beta(\mathbf{r})$ defined by the equilibrium texture. In a flare-out texture, close to the axis of the cylinder $\beta(r)$ grows

linearly, providing an approximately harmonic potential. This should cause the appearance of a series of spin-wave peaks equally spaced in frequency [6, 9, 11]. However, in the temperature and pressure region considered in this article the frequency spacing between the modes is very small. In addition, most of the absorption at high rotation velocities occurs far away from the Larmor frequency, where the degeneracy and the width of the spin-wave peaks are large. Therefore we do not expect to see any resonances and neglect their effect on the NMR line shapes.

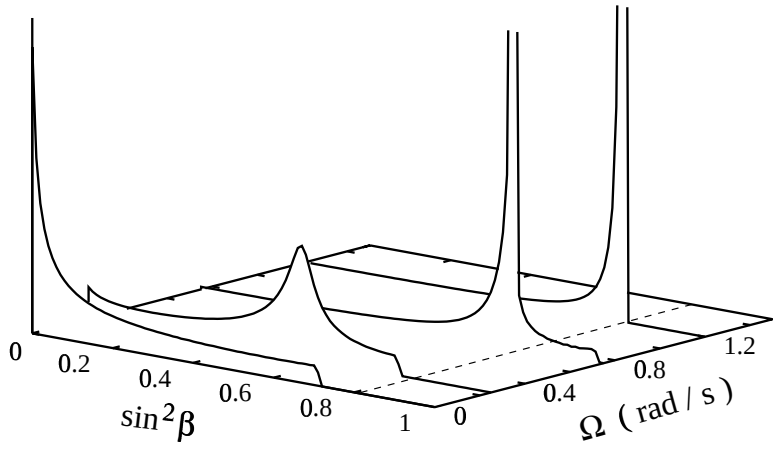

Figure 2: Numerically calculated NMR absorption line shapes for different angular velocities of rotation without line broadening effects in the vortex-free case. The radius of the cylinder $R = 2.5$ mm, $P = 2$ bar, $T = 0.9\ T_c$ and $H = 20$ mT (giving $\xi_H = 0.24\ R$, $v_D = 0.21$ mm/s).

4 Line width of the counterflow peak

In addition to the textural effects in the NMR of ^{3}He-B, there exist also other mechanisms that cause significant line broadening in the experiments. The most obvious of these is due to the fact that the external magnetic field is not entirely homogeneous over the sample. This causes a spread in the Larmor frequency, and therefore in the transverse resonance frequencies according to Eq. (7). If we assume that the field strength is spread by ΔH

from the average value H, the resulting difference in the frequencies causes a significant dephasing after a time of the order of

$$\tau_{\rm H} = \left(\omega_0 \frac{\Delta H}{H}\right)^{-1} \equiv \Gamma_{\rm H}^{-1}. \tag{9}$$

We have not determined the actual distribution of the field $\mathbf{H}(\mathbf{r})$ in the presence of superconducting wires. Instead, we assume a simple model where the inhomogeneity is taken into account by adding a term $-\Gamma_{\rm H}\mathbf{S}_\perp$ on the right-hand side of (6b), where $\mathbf{S}_\perp$ is the transverse component of the magnetization. Effectively this replaces the delta function in (8) with a Lorentzian with a width $\Delta\omega = \Gamma_{\rm H}$. The strength of the broadening is $\Gamma_{\rm H} \propto \omega_0$ and thus linearly dependent on the field strength H.

Another source of line broadening is the intrinsic Leggett-Takagi relaxation. This arises from the nonequilibrium between the normal and superfluid contributions to the total magnetization. This effect can be described by a similar term as the field inhomogeneity by introducing another damping factor [16]

$$\Gamma_{\rm LT} = \frac{1-\lambda}{\lambda} \frac{\chi_{\rm B}}{\chi_0} \frac{\Omega_{\rm B}^4}{2\omega_0^2} \tau_{\rm LT} \sin^2\beta, \tag{10}$$

where λ is a temperature-dependent number, $\lambda(T_{\rm c}) = 0$ and $\lambda(0) = 1$, χ_0 is the normal state susceptibility and $\tau_{\rm LT}$ is the Leggett-Takagi relaxation time. It should be noted that the damping strength depends on the local value of the order parameter through $\sin^2\beta$ and therefore on the position inside the cylinder. Furthermore, because of ω_0^2 in the denominator, $\Gamma_{\rm LT} \propto H^{-2}$.

There is yet a third mechanism which broadens the NMR line and which is due to spin diffusion. The broadening arises because of the movement of the atoms to locations with different resonance frequencies. This effect may be included by adding a term $D\boldsymbol{\nabla}^2\mathbf{S}_\perp$ to the right-hand side of (6b), where D is the diffusion constant. However, in the particular case of high rotation velocities spin diffusion may be ignored because the frequency gradients driving the diffusion are small due to the homogeneity of the order-parameter texture (Fig. 1). It must be emphasized that this neglect is justified only in this limit.

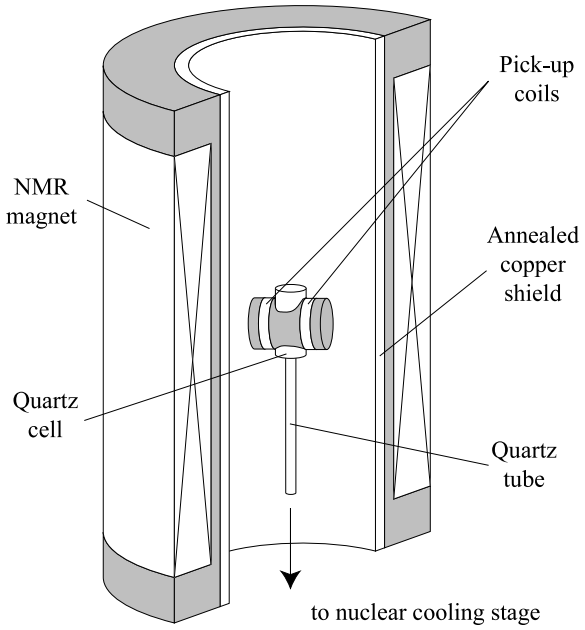

Figure 3: Liquid ^{3}He sample container and NMR setup. The NMR measurements were performed on a cylindrical quartz container with a volume of 0.1 cm^3, filled with ^{3}He at 2.0 bar pressure. The solenoidal NMR magnet is used to produce static fields from 10 to 30 mT with a field inhomogeneity of $\Delta H/H \sim 2 \cdot 10^{-4}$.

5 Experimental setup

The NMR spectrum depends on several externally controlled parameters such as temperature, pressure, magnetic field, rotation velocity, and the number of vortex lines which may be present in the container. We performed a series of measurements where all of these parameters have been varied, except for the pressure, which was fixed to $P = 2.0$ bar.

The ^{3}He NMR sample is contained in a small quartz cylinder (Fig. 3) and is refrigerated with nuclear demagnetisation of copper. An orifice in the bottom plate of the cylinder connects the sample cell to a tube which provides the thermal link to the sintered heat exchanger on the nuclear cooling stage [17]. Precooled with a standard ^{3}He-^{4}He dilution unit to a

temperature of $\approx$ 15 mK in a high magnetic field $\approx$ 8 T, the adiabatic demagnetisation of copper allows to cool the sample below the superfluid transition (T_c = 1.18 mK at 2.0 bar). All the measurements have been performed within the temperature range from 0.7 T_c to T_c. The axis of the quartz cylinder is parallel to the axis of rotation of the cryostat. The smooth surfaces of the quartz increase the critical velocity for vortex formation to $\Omega > 3.5$ rad/s. The size of the orifice in the cylinder was chosen to be small ($\approx$ 0.5 mm in diameter) to avoid the leakage of vortices from the sinter volume into the sample chamber.

The NMR spectrometer is based on a resonant circuit in which the inductive part is a superconducting coil surrounding the ^{3}He sample. The excitation of the resonance circuit was weakly coupled either by means of a small capacitance or by a separate excitation coil. In both cases, provided that the condition $|Q\xi\chi(\omega)| \ll 1$ is fulfilled, the voltage drop V_s measured at the output of the resonant circuit is proportional to the dynamic susceptibility $\chi(\omega)$ of the helium sample. Here the quantity Q is the quality factor of the resonant circuit, and ξ is the filling factor which determines the coupling between the pick-up coil and the sample. The signal V_s is amplified with a preamplifier operating at liquid-helium temperature and the tank capacitor and the pick-up coil were thermally anchored to the nuclear stage. Since the excitation frequency is fixed by the inductance of the pick-up coil and the tank capacitance, the spectra are measured in practice by sweeping the NMR field. Provided that the sweep range $H_2 - H_1$ is small compared to the field $H_0 = \omega_0/\gamma$, when Ω_B is known, one can use Eq. (7) to establish a one-to-one correspondence between H and ω, and then reconstruct the NMR spectrum as a function of ω. In our case, $(H_2 - H_1)/H_0$ never exceeded 1.5%.

The measurements were performed at three frequencies 380200, 687670, and 1027980 Hz, corresponding to ^{3}He Larmor frequencies in magnetic fields 11.73, 21.21, and 31.70 mT, respectively. Two different pick-up-coil and sample container arrangements were used in our measurements: one with a cell radius of 2.5 mm and height 7 mm (at 11.73 mT and 21.21 mT, with $Q = 2000$) and another with a cell radius of 2 mm and height 8 mm (31.70 mT, $Q = 13500$). The corresponding numerical calculations were performed at 10 mT, 20 mT, and 30 mT instead of the exact experimental field values.

The static NMR field was produced with a superconducting compensated solenoid parallel to the axis of the cylinder. Fig. 3 shows the Helmholtz configuration used in the 31.70 mT experiment. In this case, the same coil was used to detect the signal as well as to generate the rf field. In the two

experiments at lower fields, separate orthogonal coils were used for excitation and detection. Both of these were of saddle-shape geometry. In all cases, superconducting coils were used in order to achieve a good quality factor Q. To further improve the Q value, a shield of annealed copper was installed inside the NMR magnet to prevent rf field losses in surrounding metals.

In practice, the sample regions which are outside the pick-up coil do not contribute significantly to the signal. Therefore, the top and bottom plates of the sample container need not be very far outside the coil in order for our one-dimensional theoretical model (Sect. 7) to be applicable. For example, in the measurements at 31.7 mT, the pick-up coil consisted of two circular halves of 5 mm diameter and 5 mm separation between the halves. In this configuration, the contribution of the two 1.5 mm long sections outside the coil is only 5% of that in the central 5 mm long section. This is below the uncertainty of our measurements.

6 NMR measurements

In order to compare the field homogeneities, the NMR spectrum was measured in the normal phase just above the superfluid transition temperature. The value of the line width is obtained by fitting a Lorentzian line to the measured spectrum. At the two lower fields, we find that the relative inhomogeneity $\Delta H/H$ is roughly the same. The shape of the signals is similar and the full width at half maximum FWHM is about $3.5 \cdot 10^{-4}$. The line shape at 31.7 mT, measured with a different pick-up coil geometry, is somewhat different and slightly broader: FWHM $\approx 5 \cdot 10^{-4}$. The inhomogeneity is determined by the NMR magnet itself and also, we believe, by the presence of the superconductor in the pick-up coil, which can induce a distortion of the NMR field.

In the superfluid state the frequency shift induced by the dipole interaction leads to a redistribution of the resonance frequencies. Typical NMR spectra are shown in Fig. 4. The absorption χ''/χ_0 is plotted as a function of the frequency $\omega/2\pi$. Assuming that the transmission factor of the spectrometer is constant for a given experimental setup, it is possible to express the signal amplitude as

$$\frac{\chi''(\omega)}{\chi_0} = \frac{\omega_0 \pi}{2} \frac{\chi_{\rm B}(T)}{\chi_0} \frac{V_{\rm s}(\omega)}{\int V_{\rm s}(\omega') d\omega'}, \tag{11}$$

where $\chi_{\rm B}(T)/\chi_0$ is defined as the ratio of the total integrated NMR absorp-

tions at the measuring temperature T and at T_c [18]. It can be obtained experimentally from the ratio of the integrated signal voltages $V_s(\omega)$ at the measuring temperature and just above the transition temperature:

$$\frac{\chi_B(T)}{\chi_0} = \frac{\left(\int V_s(\omega')d\omega'\right)_T}{\left(\int V_s(\omega')d\omega'\right)_{T_c}} \tag{12}$$

We checked that these measurements are in reasonable agreement (within $\pm 5\,\%$) with the theoretical weak-coupling susceptibility [3] taking into account the trivial strong-coupling correction.

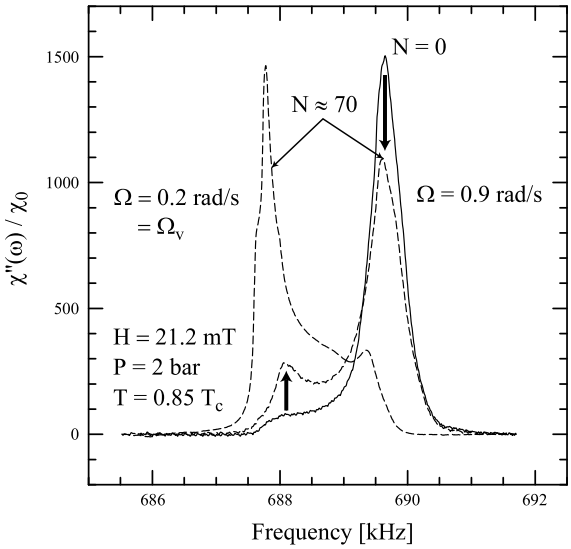

Figure 4: Typical NMR spectra measured below T_c. The dashed lines show two spectra obtained with the same number of vortices $N \approx 70$, but at two different rotation velocities 0.2 and 0.9 rad/s. The spectrum with the large peak on the left at the Larmor edge ($\omega_0/2\pi = 687\,670$ Hz) represents the equilibrium vortex state $\Omega = \Omega_v$. In the two other cases $\Omega > \Omega_v$ and the peak is generated by vortex-free counterflow at $\sin^2\beta = 4/5$. The two latter peaks are measured at the same rotation velocity $\Omega = 0.9$ rad/s, but for two different numbers of vortices. The arrows show the change in the peak heights when, at a fixed velocity $\Omega = 0.9$ rad/s, in the vortex-free state, we add 70 vortex lines into the cell.

The two states with $N \approx 70$ vortex lines plotted in Fig. 4 are obtained by cooling the ^{3}He sample through the superfluid transition while the cryostat is rotating at the velocity $\Omega = 0.2$ rad/s. The number of vortices is then equal to the equilibrium number

$$N_{\rm eq} = N_0 \left(1 - \sqrt{\frac{\Omega^*}{\Omega}} \right), \tag{13}$$

where $N_0 = 2\pi\Omega R^2/\kappa$ is the maximum number of vortex lines in the continuum limit, and Ω^* accounts for a narrow vortex-free region between the cylinder wall and the central vortex bundle [19]. The value of Ω^* is ≈ 0.032 rad/s, the quantum of circulation κ is $6.61 \cdot 10^{-8}$ m^2/s, and the number of circulation quanta per vortex is one.

In the rotating equilibrium state ($\Omega = \Omega_{\rm v}$) the NMR absorption is accumulated in a large peak just above the Larmor frequency ω_0 (Fig. 4). If Ω is increased, when the temperature is below $T_{\rm c}$, the absorption is shifted to higher frequency in the counterflow peak ($\Omega = 0.9$ rad/s in Fig. 4). A comparison is made to the counterflow peak in the vortex-free state ($\Omega_{\rm v} = 0$) by bringing the rotation to a complete stop and then increasing it back to 0.9 rad/s. The change in the height of the counterflow peak ($\sin^2\beta = 4/5$) per vortex can be estimated to be

$$\frac{\delta \bar{V}_{\rm s}}{\delta N} = \frac{\bar{V}_{\rm s}(N=0) - \bar{V}_{\rm s}(N>0)}{N}. \tag{14}$$

This linear approximation is justified when $N \ll N_{\rm eq}$. Then the peak height $\bar{V}_{\rm s}(N)$ depends linearly on N [19]. Single-vortex resolution is achieved when $\delta\bar{V}_{\rm s}/\delta N$ exceeds the noise in $V_{\rm s}(\omega)$ [2]. In practice this has been the case at high temperatures: $T_{\rm c} > T \gtrsim 0.80\ T_{\rm c}$. In the B phase several effects lead to the decrease of the height of the counterflow absorption peak with decreasing temperature: the decreasing susceptibility $\chi_{\rm B}$, and the increasing $\Omega_{\rm B}$ and $\tau_{\rm LT}$, which both broaden the NMR line shape. To extend single-vortex measurement to lower temperatures, one should understand how to maximize the signal in Eq. (14).

Fig. 5 shows that the counterflow peak height increases when the rotation velocity is increased. This growth is expected to saturate in the high velocity region when $v \gg v_{\rm D}$. Although the peak height shows to be bending over in that region, it does not seem to saturate as fast as expected according to the calculations (see Sect. 8, Fig. 7). We checked that the integrated absorption intensity remained constant during the measurement while the line width

was decreasing as a function of Ω. So, it can be deduced that the increase in the peak height is only caused by the narrowing of the NMR line, as Ω is increased.

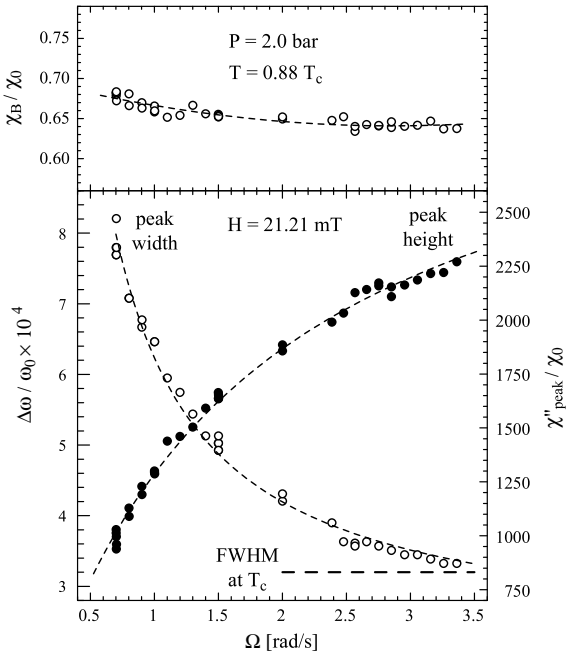

Figure 5: Height and width (FWHM) of the counterflow peak as a function of the rotation velocity. The width is normalized to the magnetic field and can be compared to the line width at T_c. The upper plot shows the integrated absorptions of the measured spectra normalized to that at T_c. The total absorption stays almost constant during the measurements and provides a control signal on the quality of temperature stabilization. The dashed lines are guides to the eye.

In all the experiments, the normalized temperature T/T_c is deduced from the measurement of Ω_B. The latter is obtained from the measured frequency shift of the counterflow peak by setting $\sin^2\beta = 4/5$ in Eq. (7). The calibration used for $\Omega_B(T)$ is an interpolation of the data obtained by Hakonen et al.[6] The function used to fit their data is

$$\Omega_{\rm B}^2 = (2\pi)^2 \left[A \left(1 - \frac{T}{T_{\rm c}} \right)^2 + B \left(1 - \frac{T}{T_{\rm c}} \right) \right] \frac{T}{T_{\rm c}}, \tag{15}$$

where the coefficients A and B are pressure dependent. The interpolation gives $A = 8.934 \cdot 10^{10}$ Hz^2 and $B = 2.301 \cdot 10^{10}$ Hz^2 at 2.0 bar pressure. It can be assumed reliable only at high temperatures $T > 0.7 T_{\rm c}$.

7 Calculation of line shape

In order to calculate the NMR line shape, we find numerically the equilibrium order-parameter texture in the cylinder. Since the pick-up coil probes primarily the central part of the sample container, we may neglect the influence of the top and bottom plates (that is, the z dependence) to a good approximation and consider the limit of an infinitely long cylinder. Because the textures are axisymmetric, we end up with a one-dimensional problem, with α and β being only functions of the distance r from the axis. In the calculations we assume the order parameter to be defined at M equidistant points along the cell radius. We replace the free energy terms (1)-(4) with their discretized counterparts. This leads to a function of $3M$ variables (the components of the vector $\widehat{\mathbf{n}}$ at M points) which is minimized. In order to avoid singular, coordinate-system dependent behaviour we use $\widehat{\mathbf{n}} = (\widehat{n}_r, \widehat{n}_\phi, \widehat{n}_z)$ as a basic variable (with the constraint $\widehat{n}_r^2 + \widehat{n}_\phi^2 + \widehat{n}_z^2 = 1$) rather than the angles α and β.

After determining the minimum-energy texture, the NMR spectrum without damping, $f(\omega)$, can be obtained using Eqs. (7) and (8). The relaxation effects are included by taking a convolution of $f(\omega)$ with a Lorentzian

$$F(\omega) = \frac{1}{\pi} \int {\rm d}\omega' \frac{\Gamma_{\rm tot}(\omega')}{(\omega - \omega')^2 + \Gamma_{\rm tot}^2(\omega')} f(\omega'), \tag{16}$$

where $\Gamma_{\rm tot}(\omega') = \Gamma_{\rm H} + \Gamma_{\rm LT}(\omega')$. It should be noted again, that $\Gamma_{\rm LT}$ in Eq. (10) is different for different frequencies and therefore is a function of ω'. The as yet unspecified values of $\Delta H/H$ and $\tau_{\rm LT}$ are determined by fitting to the measured line shape.

8 Comparison of measurement and calculation

The experimental NMR data was compared with numerical calculations using the following procedure: first the corresponding minimum-energy order-

parameter texture was determined using the one-dimensional model as explained in the previous section. The effect of magnetic-field inhomogeneity was taken into account by using the measured line shapes in the normal phase. The value of $\Delta H/H$ was chosen so that the corresponding Lorentzian would resemble the true line shape as closely as possible. As the next step, the value of $\tau_{\rm LT}(T)$ was chosen by fitting so that the resulting line shapes using Eq. (16) would be in reasonable agreement with the experimental ones (Fig. 6). The magnetic field inhomogeneity only depends on the experimental setup and the value of the field, but $\tau_{\rm LT}$ must be fitted separately for all different values of temperature. The majority of the experimental data between 0.7 $T_{\rm c}$ and $T_{\rm c}$ could be explained by choosing the value of $\tau_{\rm LT}$ to be of the order of 0.2 μs, with an uncertainty bracket of $\pm$ 0.1 μs. In the limit $T \to T_{\rm c}$, $\tau_{\rm LT}$ should approach the quasiparticle scattering time in the normal state when defined appropriately [20]. Our results are in reasonable agreement with the scattering time corresponding to the thermal conductivity, 0.34 μs [21]. The Leggett-Takagi relaxation time has been measured directly in Ref. [22] at 29 bar using pulsed NMR techniques. This data in the temperature range $T > 0.7T_{\rm c}$ gives $\tau_{\rm LT} \sim (0.15 - 0.20)$ s.

In all following figures both the measured and calculated line shapes are expressed as functions of a dimensionless variable x and multiplied with an overall constant,

$$\tilde{F}(x) \equiv \frac{\Omega_{\rm B}^2}{2\omega_0}\, F(\omega), \quad x \equiv \frac{2\omega_0}{\Omega_{\rm B}^2}(\omega - \omega_0), \tag{17}$$

so that the integrated area under the absorption curve $\int {\rm d}x\tilde{F}(x) = 1$. In the absence of relaxation $x = \sin^2\beta$. The connection with the measured signal voltage $V_{\rm s}(\omega)$ is given by $\tilde{F} = (\Omega_{\rm B}^2/2\omega_0)V_{\rm s}(\omega)/\int {\rm d}\omega' V_{\rm s}(\omega')$.

Fig. 7 shows how the normalized counterflow peak height depends on Ω for the three different magnetic fields used in our measurements. We find reasonable agreement between experiment and theory. However, it can be seen that the measurements show a somewhat stronger velocity dependence than our theoretical model. This problem seems to be more pronounced at small magnetic fields. The main uncertainty in this comparison of calculation to experiment are the exact values of the various parameters, in particular that of $v_{\rm D}$. By varying $v_{\rm D}$ better agreement can be generated, but here we restrict the comparison to the values suggested in Ref. [4].

In Fig. 8 the dependence of the peak height on the number of vortices in the vortex bundle is presented. Again, the measured values show a stronger

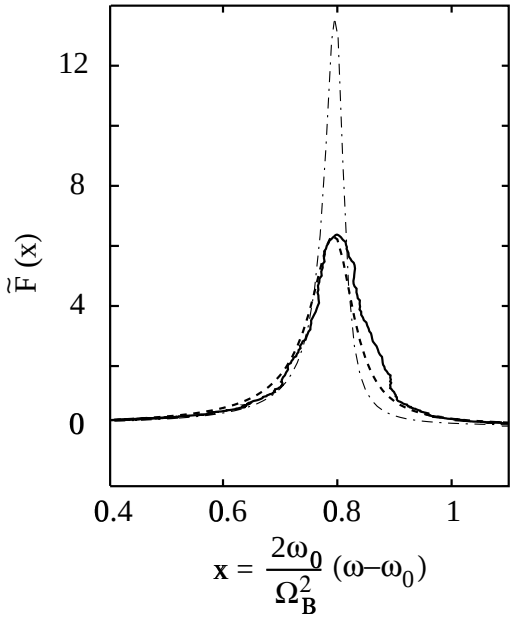

Figure 6: Measured (full line) normalized NMR absorption spectrum in the vortex-free state at $H = 11.7$ mT, $T = 0.91\ T_c$, and $\Omega = 1.5$ rad/s. In the calculated line shapes (dashed curves) $\xi_H = 0.45\ R$ and $v_D = 0.21$ mm/s. The magnetic field inhomogeneity $\Delta H/H = 1.65 \cdot 10^{-4}$ was determined from the normal phase signal. The best fit with respect to the Leggett-Takagi relaxation time was achieved choosing $\tau_{LT} = 0.15\ \mu$s and the corresponding line shape is shown as a dashed line. Also, the calculated spectrum without Leggett-Takagi relaxation ($\tau_{LT} = 0$) is shown as a dash-dotted line. Only the frequency region well above the Larmor frequency is shown since essentially no NMR absorption remains in the region $x < 0.4$.

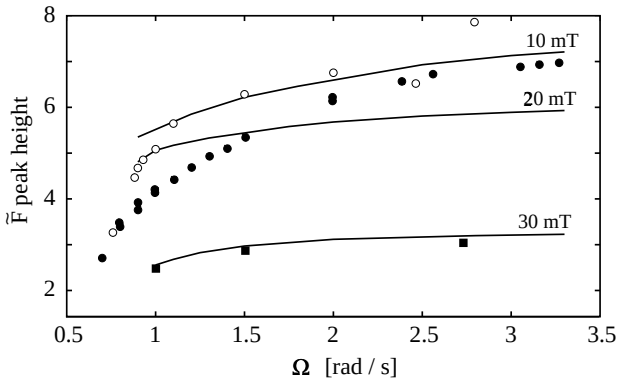

Figure 7: The normalized counterflow peak height, max $\tilde{F}(x)$ in Eq. (17), as a function of Ω in the vortex-free state. The experimental results are at H = 11.7 mT, $T = 0.895\ T_{\rm c}$ (open circles); H = 21.2 mT, $T = 0.88\ T_{\rm c}$ (filled circles); and H = 31.7 mT, $T = 0.8\ T_{\rm c}$ (filled squares). In the calculations the following values were used: $\Delta H/H = 1.65 \cdot 10^{-4}$, $\tau_{\rm LT} = 0.16\ \mu$s, $\xi_{\rm H} = 0.5\ R$, and $v_{\rm D} = 0.21$ mm/s (10 mT); $\Delta H/H = 1.4 \cdot 10^{-4}$, $\tau_{\rm LT} = 0.16\ \mu$s, $\xi_{\rm H} = 0.27\ R$, and $v_{\rm D} = 0.20$ mm/s (20 mT); and $\Delta H/H = 2.7 \cdot 10^{-4}$, $\tau_{\rm LT} = 0.3\ \mu$s, $\xi_{\rm H} = 0.32\ R$, and $v_{\rm D} = 0.18$ mm/s (30 mT).

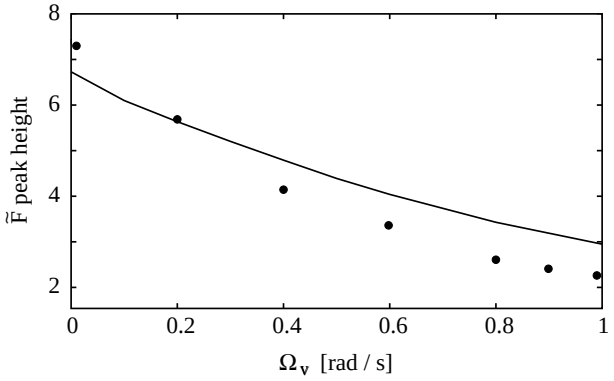

Figure 8: Measured (filled circles) and calculated (curve) normalized counterflow peak height as a function of the number of vortex lines or $\Omega_{\rm v}$ for $H \approx 10$ mT, $T = 0.9\ T_{\rm c}$, $\Omega = 2$ rad/s, $\xi_{\rm H} = 0.48\ R$, and $v_{\rm D} = 0.21$ mm/s. $\Omega_{\rm v} = 1$ rad/s corresponds to ≈ 600 vortex lines. In calculations the values $\Delta H/H = 1.65 \cdot 10^{-4}$ and $\tau_{\rm LT}$= 0.2 μs were used.

dependence on the vortex number than the calculated ones. Finally, the temperature dependence of the peak height is shown in Fig. 9.

Keeping a constant value of $\tau_{\rm LT}$ leads to good agreement between theory and experiment, suggesting an approximately constant value of $\tau_{\rm LT}$ in the temperature range considered. However, it should be emphasized that at 30 mT magnetic-field inhomogeneity is the dominant line-broadening mechanism. By dividing the difference in peak heights with the number of vortex lines we get from Fig. 9 according to Eq. (14) the single-vortex signal as a function of temperature. This is a rapidly decreasing quantity towards lower temperatures, which is not apparent from Fig. 9 where the peak heights are multiplied by the factor $\Omega_{\rm B}^2(T)$ (Eq. 17).

For maximizing the single-vortex signal the choice for the magnitude of the external magnetic field H was also investigated. In Fig. 10 the normalized counterflow peak height from the calculations has been presented as a function of H in the vortex-free case and also with 100 vortex lines. The optimum resolution in the peak height and in its change per vortex line is achieved slightly above 10 mT. This value agrees also with experimental observations [23]. It should be kept in mind that in Fig. 10 the normalized counterflow peak height is plotted. The actual measured signal voltage

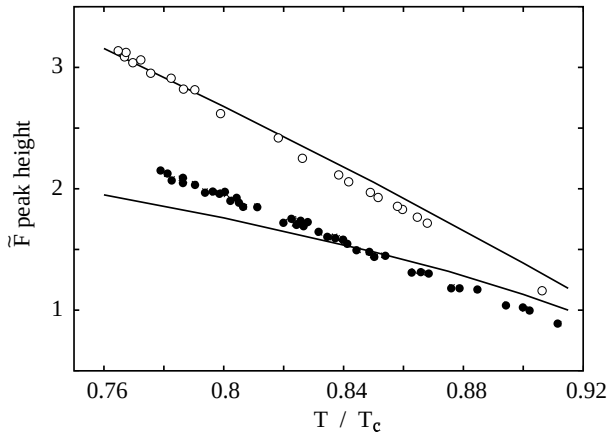

Figure 9: Measured (circles) and calculated (curves) normalized counterflow peak height as a function of temperature for $H \approx 30$ mT and $\Omega = 1.5$ rad/s. Open circles and the upper curve correspond to the vortex-free state and filled circles and the lower curve to a state with $\Omega_{\rm v} = 0.5$ rad/s (~ 190 vortex lines). In calculations the values $\Delta H/H = 2.7 \cdot 10^{-4}$ and $\tau_{\rm LT} \approx 0.3$ μs were used.

scales differently with $\omega = \gamma H$. According to Eq. (17) the signal voltage is $V_{\rm s}(\omega) = (2\omega/\Omega_{\rm B}^2)\tilde{F}\int V_{\rm s}(\omega')d\omega' \propto \omega Q\xi\chi''(\omega)\tilde{F} \propto \omega^{2+\delta}\tilde{F}$, where $\delta \leq 1$ depending on how Q scales with frequency.

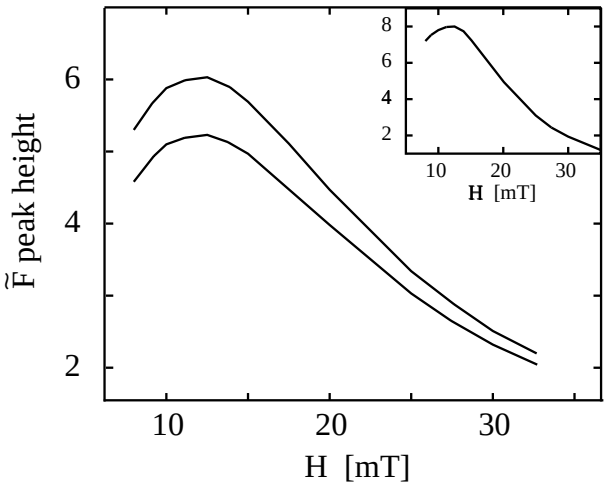

Figure 10: Calculated normalized counterflow peak height, as a function of external magnetic field strength H for $\Omega = 1.5$ rad/s, $T = 0.9\ T_{\rm c}$ (giving $v_{\rm D} = 0.21$ mm/s) and the cylinder radius $R = 2.5$ mm. The upper curve corresponds to the vortex-free state and the lower to a case with 100 vortex lines. The values $\Delta H/H = 1.5 \cdot 10^{-4}$ and $\tau_{\rm LT} = 0.2\ \mu$s were used. The insert shows the reduction in the peak height for one vortex line in the same units, but multiplied by 1000.

9 Calculation in two dimensions

In order to justify our use of a one-dimensional model we have also performed numerical calculations on a cylinder with a finite length. Since we continue considering only flare-out textures with axial symmetry, these calculations take place in a two-dimensional grid with z as a new space coordinate. The texture problem is a straightforward generalization of the one-dimensional case. The effect of the top and bottom plates of the cylinder is to reduce the counterflow peak height. This is because the surface energy (3) at the plates is minimized by having $\beta = 0$. Therefore, compared to the infinitely-long

cylinder model, part of the absorption is transferred from the counterflow region to the Larmor region. We estimated the size of this effect by collecting the texture data at a fixed value of z and forming the corresponding (one-dimensional) NMR spectrum. In Fig. 11 we have presented the counterflow peak heights of these spectra as a function of the height z in the cylinder. It can be seen that, as expected, the effect of the end plates is observable only within a distance of $\sim \xi_{\rm H}$ (≈ 1 mm) from the ends. This is the first calculation which provides an estimate of the effects of having a finite container length.

The NMR absorption in the counterflow peak, if expressed per unit length of the sample cylinder, is much reduced in the situation of Fig. 11 from that of the infinitely long cylinder. Assuming that each volume element contributes equally to the measured absorption, for the 7 mm long cylinder in Fig. 11 the counterflow peak is smaller by ~ 15 %. Such a measurement requires a pick-up coil which is larger than the sample container. In practice, to maximize the filling factor of the ^{3}He sample within the detection coil, the inductance is wound tightly around the central section of the sample container, such that the cylinder extends outside the coil at both ends. From Fig. 11 we note that to realize the true flare-out texture of the infinitely long cylinder model within the coil it is sufficient if the container extends ~ 2 mm beyond the pick-up coil at both ends. As discussed in Sect. 5, the contribution to the total absorption signal from the sample regions outside the pick-up coil is small. Thus the influence from the end sections outside the coil with the modified texture may be neglected.

10 Conclusions

In this work we presented a model which explains the NMR line shape in a rotating cylinder and particularly as a function of the magnitude of the axially oriented external magnetic field. The line shape is determined by textural effects and broadening due to magnetic-field inhomogeneity (dominant at high magnetic fields) and Leggett-Takagi relaxation (dominant at low magnetic fields). We have concentrated on high rotation velocities in order to be able to neglect the effect of spin diffusion and to have a simple line shape. The results show reasonably good agreement with experiment and explain how the height of the NMR counterflow peak varies as a function of the angular velocity of rotation, external magnetic field strength, number of vortices, and temperature. The largest deviations between the-

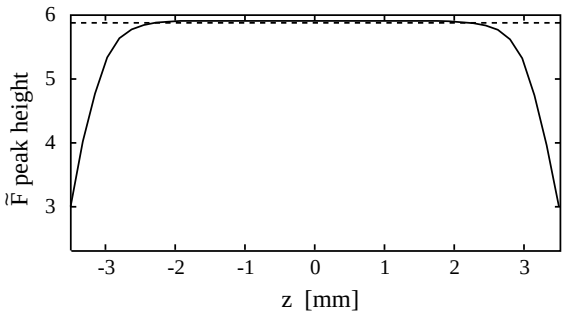

Figure 11: The counterflow peak height as a function of z in a cylinder of 2.5 mm radius and 7 mm height. $T = 0.81\ T_c$, $P = 2$ bar, $\Omega = 1.2$ rad/s, $H = 20$ mT, $\xi_H = 0.37\ R$, $v_D = 0.18$ mm/s, $\Delta H/H = 2 \cdot 10^{-4}$ and $\tau_{LT} = 0.15$ μs. The 1D calculation for the infinitely long cylinder with the same values gives the peak height ≈ 5.86 (dashed line).

ory and experiment were obtained with respect to velocity dependences: measurements showed consistently a stronger response to changes in Ω and the number of vortices. The magnitude of the discrepancy is believed to reflect the accuracy with which the various textural parameters are known for ^{3}He-B, since only Leggett-Takagi relaxation was treated as adjustable in the present calculations.

With our theoretical model we investigated the selection of the magnetic field H to get the best resolution in the determination of the number of vortex lines from the measured spectra. The optimal results were achieved in calculations by choosing H to be slightly above 10 mT, again showing good agreement with the experiments. The texture calculations were also performed for a cylinder of finite length, to estimate the role of the top and bottom plates in the NMR line shape. From the fitting procedure we were able to get an estimate for the Leggett-Takagi relaxation time, which is in order-of-magnitude agreement with previous work.

This work was funded in part by the EU-TMR programme (contract no. ERBFMGECT980122).

References

[1] P. J. Hakonen and K. K. Nummila, Phys. Rev. Lett. **59**, 1006 (1987).

[2] V. M. H. Ruutu, Ü. Parts, J. H. Koivuniemi, N. B. Kopnin, and M. Krusius, J. Low Temp. Phys. **107**, 1 (1997); Europhys. Lett. **31** (8), 449 (1995).

[3] J. W. Serene and D. Rainer, Phys. Rep. **101**, 221 (1983).

[4] E. V. Thuneberg, to be published.

[5] P. J. Hakonen, O. T. Ikkala, S. T. Islander, O. V. Lounasmaa, and G. E. Volovik, J. Low Temp. Phys. **53**, 425 (1983).

[6] P. J. Hakonen, M. Krusius, M. M. Salomaa, R. H. Salmelin, J. T. Simola, A. D. Gongadze, G. E. Vachnadze, and G. A. Kharadze, J. Low Temp. Phys. **76**, 225 (1989).

[7] A. J. Leggett, Rev. Mod. Phys. **47**, 331 (1975).

[8] W. F. Brinkman, H. Smith, D. D. Osheroff, and E. I. Blount, Phys. Rev. Lett. **33**, 624 (1974).

[9] H. Smith, W. F. Brinkman, and S. Engelsberg, Phys. Rev. B **15**, 199 (1977).

[10] W. F. Brinkman and M. C. Cross, in *Progress in Low Temperature Physics*, Vol. VIIA, ed. D. F. Brewer (North Holland, 1978), p. 105.

[11] D. D. Osheroff, Physica B **90**, 20 (1977).

[12] K. K. Nummila, P. J. Hakonen, and O. V. Magradze, Europhys. Lett. **9**, 355 (1989).

[13] J. S. Korhonen, A. D. Gongadze, Z. Janú, Y. Kondo, M. Krusius, Yu. M. Mukharsky, and E. V. Thuneberg, Phys. Rev. Lett. **65**, 1211 (1990).

[14] A. D. Gongadze, G. E. Gurgenishvili, and G. A. Kharadze, Fiz. Nizk. Temp. **7**, 821 (1981) [Sov. J. Low Temp. Phys. **7**, 397 (1981)].

[15] A. J. Leggett, Ann. Phys. (USA) **85**, 11 (1974).

[16] A. J. Leggett and S. Takagi, Ann. Phys. (NY) **106**, 79 (1977).

[17] Ü. Parts, J. H. Koivuniemi, M. Krusius, V. M. H. Ruutu, and S. R. Zakazov, Physica B **194-196**, 771 (1994).

[18] D. Vollhardt, P. Wölfle, *The Superfluid Phases of Helium 3* (Taylor & Francis, London), (1990).

[19] V. M. H. Ruutu, J. J. Ruohio, M. Krusius, B. Plaçais, and E. B. Sonin, Physica B **255**, 27 (1998).

[20] P. Bhattacharyya, C. J. Pethick, and H. Smith, Phys. Rev. Lett. **35**, 473 (1975).

[21] J. C. Wheatley, Rev. Mod. Phys. **47**, 415 (1975).

[22] Yu. M. Bunkov, V. V. Dmitriev, A. V. Markelov, and Yu. M. Mukharskii, Phys. Rev. Lett. **65**, 867 (1990).

[23] R. Schanen, R. Blaauwgeers, V. B. Eltsov, M. Krusius, J. J. Ruohio, Physica B **280**, Pt. II (2000).